Highly active enzyme–metal nanohybrids synthesized in protein–polymer conjugates

Xiaoyang Li[1,5], Yufei Cao[1,5], Kai Luo[2,5], Yunze Sun[1], Jiarong Xiong[1], Licheng Wang[1], Zheng Liu[1], Jun Li[3], Jingyuan Ma[4], Jun Ge ⬤[1]*, Hai Xiao ⬤[3]* and Richard N. Zare[2]*

Building a bridge between enzymatic and heterogeneous catalysis provides new cascade industrial processes for manufacturing. However, the reaction conditions of enzymatic and heterogeneous catalysis mutually cause deactivation of catalysts. Here, we overcame this challenge by developing a special protocol for the synthesis of hybrid catalysts. We utilized protein–polymer nanoconjugates as confined nanoreactors for the in situ synthesis of lipase–palladium (Pd) nanohybrids. The 0.8 nm Pd nanoparticles exhibited increased activity in racemization of (S)-1-phenylethylamine. At 55 °C, which matches the optimum temperature of lipase, the activity is more than 50 times that of commercial Pd/C. It was found that the Pd–O coordination in Pd subnanoclusters contributed to the high activity. In the dynamic kinetic resolutions of pharmaceutical intermediates (±)-1-phenylethylamine, (±)-1-aminoindan and (±)-1,2,3,4-tetrahydro-1-naphthylamine, the lipase–Pd nanohybrids displayed 7.6, 3.1 and 5.0 times higher efficiencies than the combination of commercial immobilized lipase Novozym 435 and Pd/C. The lipase–Pd nanohybrids can be reused without agglomeration and activity loss.

Homogeneous, heterogeneous and enzymatic catalysis are three types of catalytic processes used in modern chemical industry to manufacture chemicals, pharmaceuticals and materials for human society. The pursuit of integrating the three basic types of catalysis has great theoretical and practical significance in understanding catalytic mechanisms at the atomic level and in designing highly efficient hybrid catalysts with a broadly expanded reaction spectrum[1–6]. However, the reaction conditions of homogeneous, heterogeneous and enzymatic catalysis often do not match well in that the catalyst is frequently deactivated in the process. An example is that many enzymes prefer an aqueous solution at ambient temperature, whereas heterogeneous catalysts often display a high activity at a high temperature in organic solvents[7–11].

As a typical and classical example, chemoenzymatic dynamic kinetic resolution (DKR) consists of the enzymatic kinetic resolution of racemic mixtures at ambient temperature and racemization catalysed by metals, such as palladium[12–14], ruthenium[15,16], Raney nickel[17] and iridium[18], at high temperature, which originated from the pioneering works of Paetzold and Bäckvall[15], Reetz and Schimossek[12], and others. In this reaction, the enzyme catalyses the selective acylation of one enantiomer of the racemic substrates, coupled with the racemization of the unconsumed enantiomer by metal catalysts in a one-pot process. By combining the enzymatic and metal-catalytic reactions, DKR is an efficient way to overcome the limitation of enzymatic kinetic resolution alone, which has a maximal theoretical yield of only 50%. Although DKR is a promising process for manufacturing enantiomerically pure alcohol and amine derivatives with a maximal theoretical yield of 100% in one step[4], the high temperatures (70–110 °C) and organic media required by metal catalysts in this reaction usually cause serious enzyme deactivation. The chemoenzymatic DKR process represents one of the most challenging combinations of enzymatic and heterogeneous systems due to the large incompatibility of reaction conditions.

To achieve this integration, several strategies have emerged. Genetic engineering[19,20], the immobilization of the enzyme on insoluble support matrices[21] and the chemical modification of enzyme with polymers[22–25] were used to increase enzyme stability and activity under harsh conditions. The catalytic performances of metal catalysts were enhanced by dispersing metal nanoparticles (NPs) on metal oxides[26], mesoporous silica[13,27] and layered double hydroxides[28]. For example, a promising approach to construct enzyme–metal nanohybrid catalysts with a high efficiency for DKR was developed by Bäckvall group[13], in which lipase and Pd NPs were co-immobilized in cavities of siliceous mesocellular foam. However, two major challenges remain in the field of combined enzymatic and heterogeneous catalysis at low temperatures: (1) to achieve a high catalytic activity of the heterogeneous catalysts that matches the enzymatic reactions at ambient conditions and (2) to understand the catalytic pathways of heterogeneous catalysts integrated with the enzyme.

In this study, we utilized single lipase–polymer nanoconjugates as confined nanoreactors for the in situ generation of Pd NPs. This approach permits the construction of lipase–Pd nanohybrids (Fig. 1a). We succeeded in downsizing the Pd NPs from 2.5 to 0.8 nm using the confined environment created by the single protein–polymer nanoconjugate. The Pd subnanoclusters formed in the lipase–polymer nanoconjugates exhibited a markedly increased activity. At 55 °C the activity was higher than that of commercial Pd/C by more than 50 times in the racemization of (S)-1-phenylethylamine ((S)-1-PEA). We found that the presence of sufficient Pd–O coordination contributed to the size-dependent high activity of the Pd subnanoclusters. The protein–polymer nanoconjugates assisted the formation of the Pd–O coordination on the Pd subnanoclusters and stabilized the ultrasmall Pd particles. The high activity of Pd subnanoclusters at a low temperature (55 °C) matched well with the optimum temperature of lipase. This resulted in the lipase–Pd nanohybrids that displayed a 7.6 times higher efficiency than
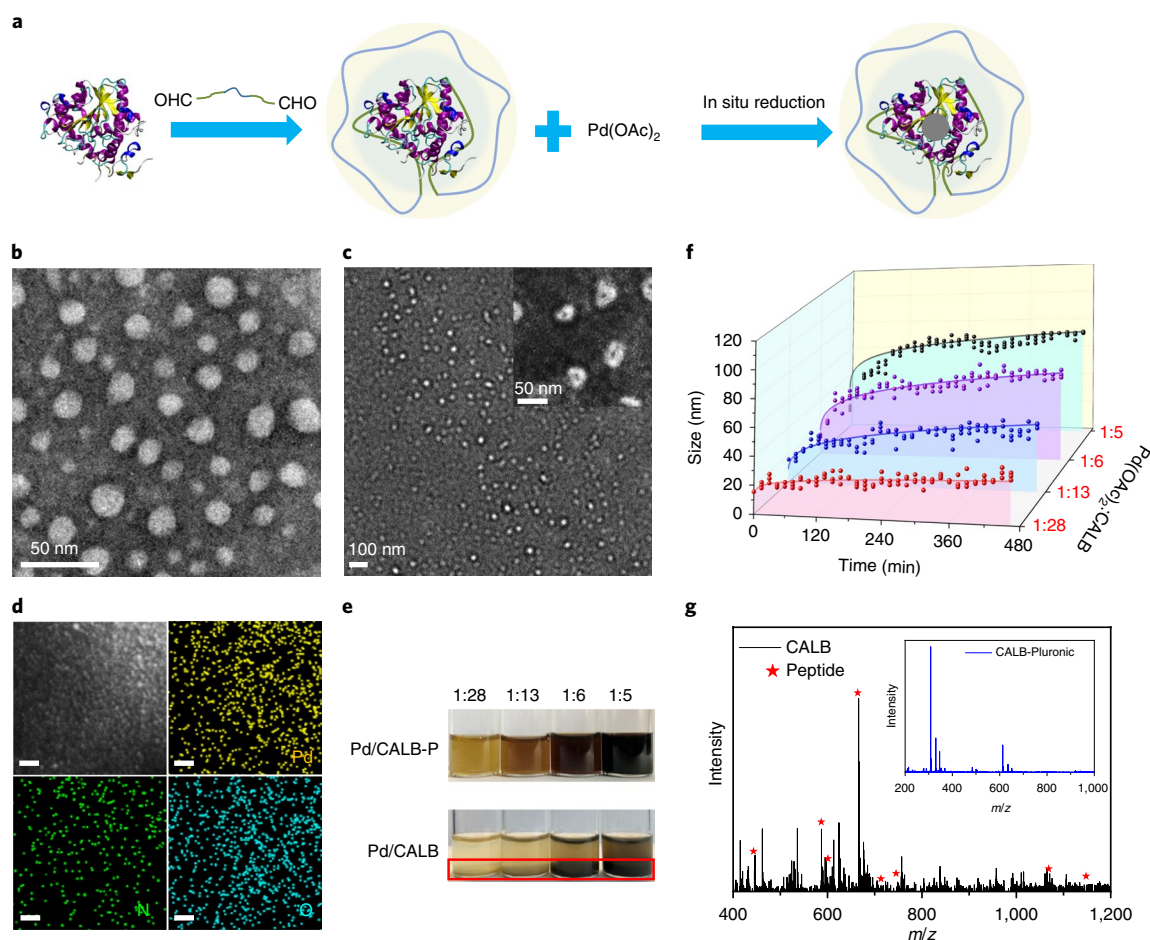
Fig. 1 | Fabrication and characterization of Pd/CALB-P nanohybrids. a, Schematic illustration of the strategy used to synthesize Pd/CALB-P via in situ reduction in single protein–polymer nanoconjugates. **b,c**, Negatively stained TEM images of CALB-P nanoconjugates (**b**) and Pd/CALB-P nanohybrids (**c**). Inset: high-resolution image of Pd/CALB-P nanohybrids in which the dark dots represent single Pd NPs generated in single protein–polymer nanoconjugates. **d**, HAADF-STEM image of Pd/CALB-P nanohybrids and the corresponding elemental mapping for Pd, N and O. Scale bars: 10 nm. **e**, Photos of reaction mixtures for the synthesis of Pd/CALB-P and Pd/CALB nanohybrids with different concentrations of CALB and Pd(OAc)$_2$ after stirring at 25 °C for 20 hours. **f**, In situ DLS assays during the synthesis of Pd/CALB-P with different weight ratios of Pd(OAc)$_2$ and CALB. **g**, The mass spectra of CALB and CALB-P (inset) digested with trypsin in the microdroplet reaction by nano-electrospray ionization.

the combination of commercial immobilized lipase Novozym 435 and Pd/C in the DKR of (±)-1-PEA. We believe that this example demonstrates the promise of a combined enzymatic and heterogeneous catalysis achieved by using protein–polymer conjugates as nanoreactors.

Results

Synthesis of enzyme–metal nanohybrids. The protein–polymer conjugates were synthesized by covalently linking *Candida antarctic* lipase B (CALB) with an aldehyde-functionalized triblock copolymer of propylene oxide and ethylene oxide (PEO–PPO–PEO) (Pluronic F-127) via a Schiff base reaction. This was confirmed by Fourier transform infrared spectroscopy (Supplementary Fig. 1). As determined by matrix-assisted laser desorption ionization time-of-flight mass spectrometry (Supplementary Fig. 2), each conjugate contained one CALB molecule attached to one Pluronic F-127 (CALB-P). The number of free amine groups on the surface of CALB and the CALB-P nanoconjugate were determined as 10 and 9, respectively (Supplementary Fig. 3). This result indicates that a single polymer chain was attached to one enzyme molecule via one end of the polymer covalently bonding with an amine group of the protein. It is highly possible that the most reactive lysine

residue on the protein surface was responsible for this conjugation (Supplementary Fig. 3b). The single protein–polymer conjugate displayed the average hydrodynamic size of 21 nm, determined by dynamic light scattering (DLS) (Supplementary Fig. 4). The negatively stained transmission electron microscopy (TEM) image (Fig. 1b and Supplementary Fig. 4) shows that the single conjugate had an average size of 13 nm in dry form, which agreed well with the results of DLS.

The Pd NPs were generated in situ on the CALB-P conjugates by the reduction of Pd^{2+} ions in an aqueous solution that contained 20% (v/v) methanol (Fig. 1a). In this process, Pd^{2+} ions may bind first in the areas that contained negatively charged amino acid residues on the protein surface, followed by a subsequent reduction by methanol[29,30] and by the reducing amino acid residues in protein[31–33]. The Pd NP was expected to grow within the confinement of the protein–polymer nanoreactor. The Pd/CALB-P nanohybrids had a similar morphology to CALB-P, and single Pd NPs were formed inside single CALB-P conjugates (Fig. 1c). Each Pd NP appeared as a black dot surrounded by white CALB-P conjugate. The high-angle annular dark-field scanning transmission electron microscopy (HAADF-STEM) image and the corresponding energy-dispersive X-ray spectroscopy mapping (Fig. 1d) also

confirmed that the Pd NPs were successfully synthesized without agglomeration in the presence of CALB-P. The in situ monitoring of the formation of Pd/CALB-P nanohybrids (Fig. 1f) in aqueous solution proved that the size (diameter) of Pd/CALB-P increased from 21 nm (the size of a single CALB-P conjugate) to 27–66 nm within 180 minutes caused by the formation of Pd NPs on CALB-P. Different input weight ratios of $Pd(OAc)_2$ and CALB resulted in different sizes of Pd/CALB-P in 180 minutes, namely 27, 41, 51 and 66 nm for ratios of 1:28, 1:13, 1:6 and 1:5, respectively. The sizes of Pd/CALB-P were maintained, without the formation of aggregates, for the rest of the five hour synthesis process (Fig. 1e,f). As a control experiment, the Pd/CALB composites were synthesized by the reduction of Pd^{2+} directly on the free CALB. The result was that large aggregates were inevitably formed. The sizes of the Pd/CALBs became large (344–608 nm) very quickly in the synthesis process (Fig. 1e and Supplementary Figs. 5 and 6). The zeta potential and size of the free CALB molecules in aqueous solution was −14.4 mV and 4 nm (Supplementary Figs. 4 and 7). After reduction of the positively charged Pd NPs on CALB molecules, because of the electrostatic interactions and incomplete coverage of Pd NPs with protein molecules, aggregates formed between the nuclei or particles due to the high surface energy of ultrafine metal crystals[34,35]. In contrast, the CALB-P nanoconjugate had a relatively neutral surface (zeta potential of −3.0 mV (Supplementary Fig. 7)) and larger molecular size (21 nm (Supplementary Fig. 4)). The aggregation of Pd NPs can be inhibited when confined within CALB-P nanoconjugates owing to the steric hindrance and shielding of electrostatic interactions. The possible configuration of Pd/CALB-P obtained by molecular dynamics simulations showed that the chain of Pluronic entangled around the protein and Pd NP was embedded in the confined space created by both protein and polymer (Supplementary Figs. 12–14). The entanglement of Pluronic around the protein was further confirmed by the nano-electrospray ionization mass spectrometry ((nanoESI)–MS). We identified eight peptides for the CALB digested by trypsin (Fig. 1g, Supplementary Fig. 17 and Supplementary Table 4). No peptide was identified in the digestion of the CALB-P nanoconjugate (Fig. 1g and Supplementary Fig. 18). It is suggested that the accessibility of trypsin towards the CALB was inhibited due to the entangled Pluronic chain (Supplementary Fig. 14). In this manner, we demonstrated that the utilization of a single protein–polymer conjugate as the template avoids the aggregation of Pd NPs during the synthesis, which is different to using the protein alone as the template.

The average size of the Pd NPs synthesized in CALB-P conjugates was readily tuned from 2.5 to 0.8 nm with narrow size distributions (2.5 ± 0.5, 2.2 ± 0.8, 1.6 ± 0.5 and 0.8 ± 0.2 nm) (Fig. 2a–d) by decreasing the concentration of $Pd(OAc)_2$ (Supplementary Table 5). The lipase–Pd nanohybrids are denoted as xPd/CALB-P, where x represents the average size of the Pd NPs in nanometres. The Pd(111) in the crystal lattice was observed as the exposed facet in each sample (Fig. 2e–h). The loading amounts of Pd in xPd/CALB-P ($x = 2.5$, 2.2, 1.6 and 0.8) were 8.0, 6.7, 4.7 and 3.6 wt%, respectively, as measured by inductively coupled plasma–atomic emission spectrometry, whereas the amounts of CALB in these samples were correspondingly 7.5, 9.7, 8.7 and 9.8 wt%, as measured by Bradford protein assay. A further decrease in the concentration of $Pd(OAc)_2$ (0.3 mg ml^{-1}) in the synthesis only resulted in a slight decrease of the Pd size to 0.7 ± 0.2 nm (Supplementary Fig. 20), whereas the loading amount of Pd greatly reduced to 0.8 wt%. Therefore, 0.8 nm was the optimized smallest size of Pd given a reasonable loading amount of Pd in the nanohybrid. HAADF-STEM images for a broader view of 0.8Pd/CALB-P and DLS results (Supplementary Figs. 21 and 22) indicated that no aggregates or large particles were formed. In addition, X-ray diffraction (Supplementary Fig. 23) confirmed a face-centred cubic palladium in the Pd/CALB-P nanohybrids. No obvious peaks of face-centred cubic Pd were found for 0.8Pd/

CALB-P and 1.6Pd/CALB-P, which possibly suggests the Pd particles in these samples were quite small.

Size-dependent activity of metal NPs in enzyme–metal nanohybrids. The catalytic properties of Pd particles in xPd/CALB-P ($x = 2.5$, 2.2, 1.6 and 0.8) were evaluated in the racemization of (S)-1-PEA (Fig. 2i). A commercial Pd/C (average diameter of Pd, 4.2 ± 1.0 nm (Supplementary Fig. 24)) was used as the reference. In a wide temperature range, xPd/CALB-P had higher activity of Pd than Pd/C. As the size of Pd decreased from 2.5 nm to 0.8 nm, the conversions of (S)-1-PEA after 0.5 h of reaction increased rapidly and exhibited maximum values when the Pd particles reached 0.8 nm. Especially with 0.8Pd/CALB-P as the catalyst at 55 °C, the conversion was more than 50 times higher than that with Pd/C as the catalyst. To investigate the size-dependent activity of Pd NPs[36], the apparent activities (calculated from the conversions at 0.5 h) were normalized according to the estimated Pd atoms on the surface (Supplementary Tables 1 and 7). The normalized activity (Supplementary Fig. 25) increased as the size of the Pd NPs decreased, which suggests a possible size-dependent activity. Au, Ag and Ru NPs with a controlled size were also synthesized in CALB-P conjugates by the same method and a similar size-dependent activity was observed (Supplementary Figs. 44–48).

To understand the size-dependent activity of Pd, the X-ray absorption fine structures (XAFS)[37] were examined. Pd K-edge X-ray absorption near-edge structures revealed the oxidation state of Pd NPs in Pd/CALB-P (Fig. 3a). In comparison with 2.5Pd/CALB-P, 0.8Pd/CALB-P shows a slight shift to a higher energy at the absorption edge, which suggests a higher content of oxidized Pd^{2+}. In the Fourier transformation of extended XAFS (FT-EXAFS), there was a notable peak at ~1.6 Å from the Pd–O contribution in both 2.5Pd/CALB-P and 0.8Pd/CALB-P (Fig. 3b). The intensity of the Pd–O peak increased, whereas that of the Pd–Pd peak (~2.5 Å) decreased as the size of the Pd NP changed from 2.5 to 0.8 nm, which suggests that more Pd–O coordination was presented in the Pd subnanoclusters. As the Pd NPs downsized from 2.5 to 0.8 nm, the number of Pd–O coordination bonds increased from 1.7 to 2.5, whereas those of Pd–Pd decreased from 3.8 to 2.9, as determined by EXAFS (Supplementary Table 8).

The surface chemical states of Pd NPs were characterized by high-resolution Pd $3d$ X-ray photoelectron spectroscopy (XPS), which were fitted with spin–orbit split $3d_{5/2}$ and $3d_{3/2}$ components (Fig. 3c). Two sets of peaks were observed in each sample, which contributed to the metallic Pd^0 and Pd^{2+} species, respectively (Supplementary Fig. 28). The amount of Pd^{2+} increased as the size decreased, which suggests more Pd atoms were exposed in smaller NPs[25]. In addition, the binding energy of Pd^0 $3d_{5/2}$ and $3d_{3/2}$ showed a redshift to a higher region when downsizing the NPs. These results indicate that more coordination of Pd^{2+} was present in the Pd subnanoclusters. In high-resolution O $1s$, N $1s$ and S $1s$ XPS (Fig. 3d, Supplementary Fig. 29), the peak at 530.5 eV for the Pd/CALB-P was ascribed to O–Pd, and no peaks that corresponded to N–Pd or S–Pd were detected. These results demonstrate that the Pd^{2+} atoms on the surface coordinated with the O atoms of the CALB-P nanoconjugates regardless of the size of Pd NPs, which is consistent with the EXAFS results.

Therefore, these XAFS and XPS results suggest that as the size of the Pd NP decreases, Pd–O bonds are formed in the Pd/CALB-P because of the increased proportion of oxidized Pd and Pd coordinated with O atoms from either the protein or polymer. This partially oxidized form of a Pd particle stabilized by the CALB-P nanoconjugates could be essential for a high activity of Pd.

The relationship between the partial oxidation and high activity of Pd subnanoclusters in Pd/CALB-P was investigated via density functional theory (DFT) calculations. Based on the results of EXAFS, we constructed a partially oxidized model with the O atoms
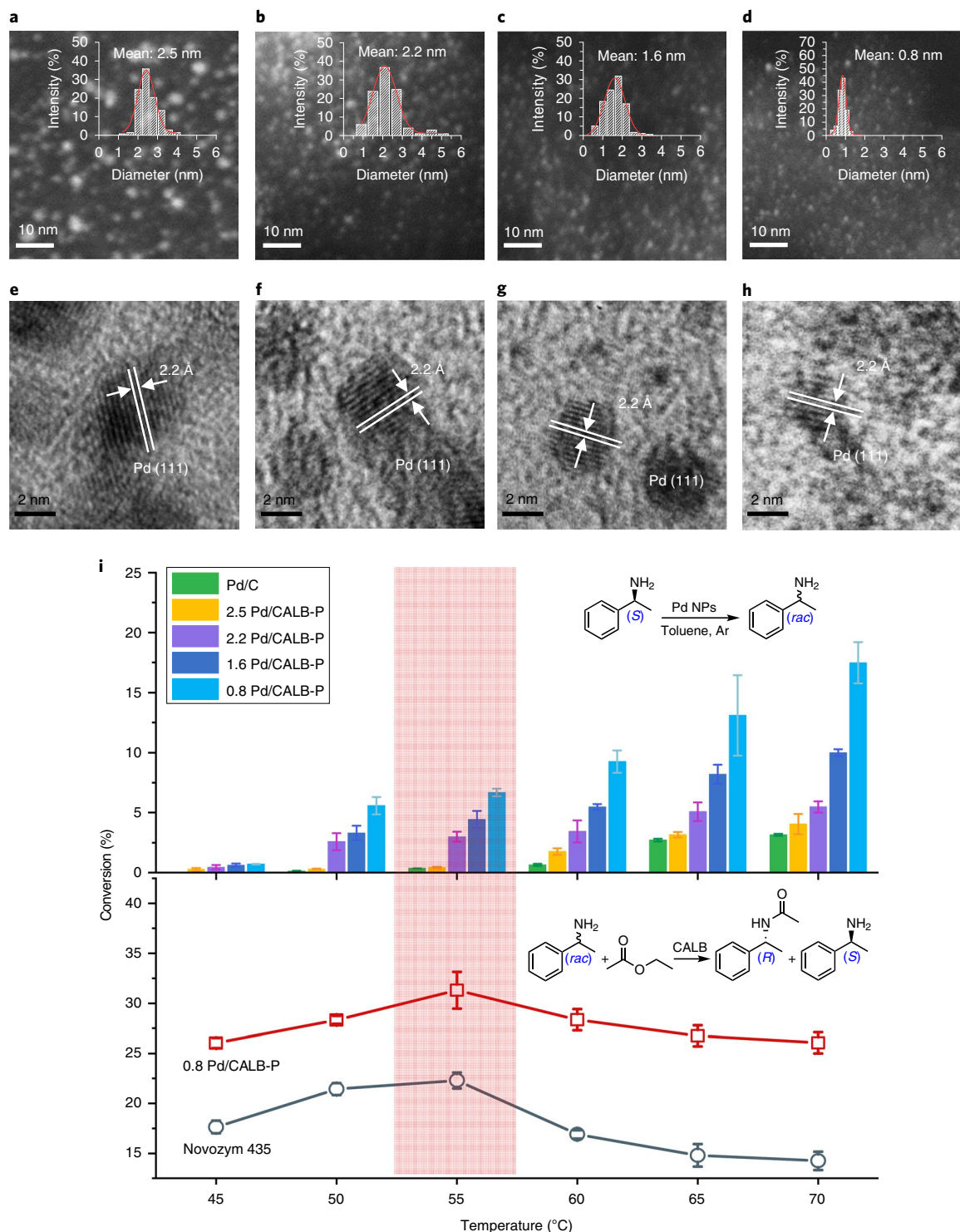
Fig. 2 | Size and activity of Pd/CALB-P nanohybrids. a–h, Pd/CALB-P nanohybrids with Pd NPs of different sizes. HAADF-STEM and the corresponding HR-TEM images of 2.5Pd/CALB-P (**a** and **e**), 2.2Pd/CALB-P (**b** and **f**), 1.6Pd/CALB-P (**c** and **g**) and 0.8Pd/CALB-P (**d** and **h**). The sizes of the Pd NPs were calculated using software Nano Measurer 1.2 and the numbers of particles were counted in 2.5Pd/CALB-P, 2.2Pd/CALB-P, 1.6Pd/CALB-P and 0.8Pd/CALB-P were 143, 101, 176 and 110, respectively. **i**, Top: catalytic performance of xPd/CALB-P at different temperatures for the Pd-catalysed racemization of (S)-1-PEA (conditions: 0.4 mmol (S)-1-PEA and 2 ml of toluene under an argon atmosphere, with the conversion calculated as $(n_0 - n_t)/n_0$, where n_0 and n_t stand for the amounts of (S)-1-PEA at 0 h and 0.5 h, respectively; all the catalysts contained the same amount of Pd, 0.64 mg). Bottom: the lipase-catalysed kinetic resolution of 1-PEA (conditions: 0.20 mmol racemic 1-PEA, 0.60 mmol ethyl acetate and 2 ml of toluene for 1 hour; all the catalysts contained the same amount of CALB, 3.6 mg). Each data point and error bar represents the mean and s.d. from at least three independent measurements.

inserted into the tetrahedral centres between the first two Pd layers on the surface (Fig. 4a and Supplementary Fig. 30). Previous studies showed that the imine intermediate is present in the pathway of the Pd-catalysed racemization of (S)-1-PEA[16,38]. Thus, we investigated a reaction pathway (Fig. 4b) in which (S)-1-PEA is first adsorbed on the Pd(111) surface, then transforms to the imine intermediate and
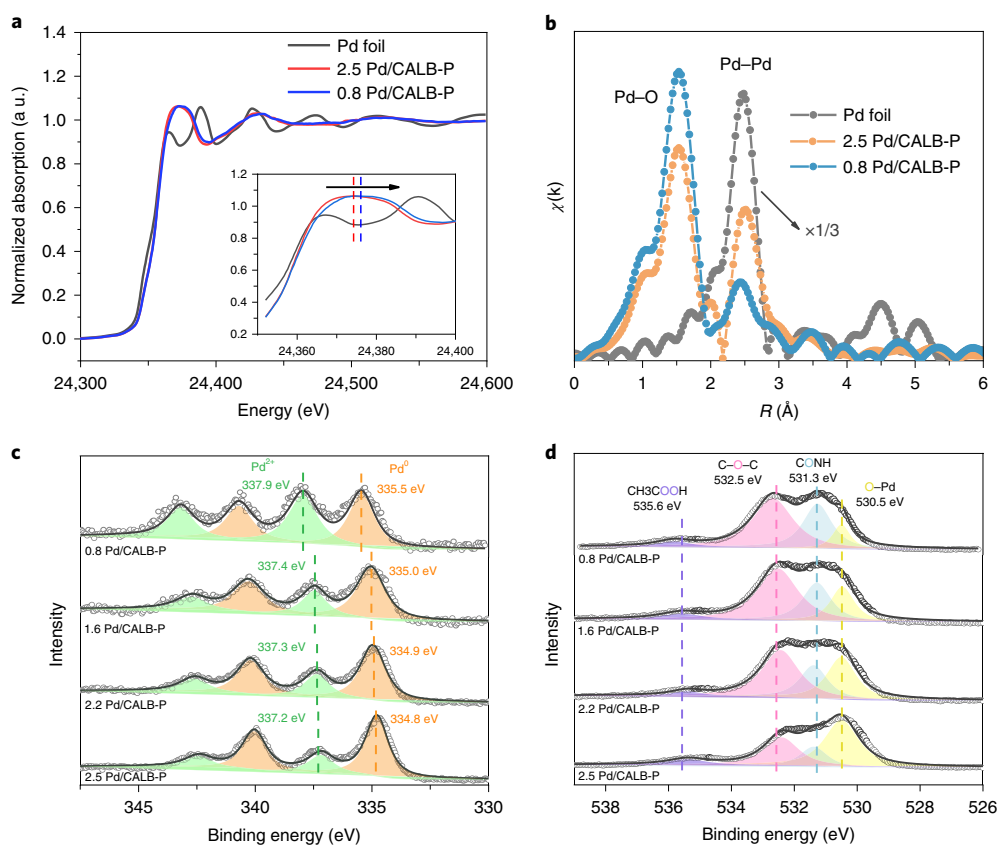
Fig. 3 | Analysis of the coordination of Pd. a, X-ray absorption near-edge structures (XANES) of the Pd K-edge for 0.8Pd/CALB-P and 2.5Pd/CALB-P, with the Pd foil used as a reference. Inset: the magnification of the white lines. **b**, Fourier transformed (FT) k^2-weighted $\chi(k)$-function of the EXAFS spectra of 0.8Pd/CALB-P, 2.5Pd/CALB-P and Pd foil in radial distance (R) at the Pd K-edge. **c,d**, High-resolution Pd 3d XPS spectra (**c**) and O 1s XPS spectra (**d**) of xPd/CALB-P.
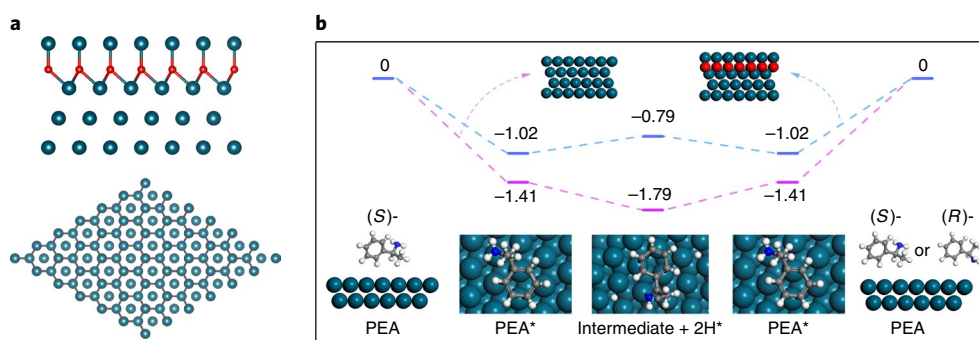

Fig. 4 | Theoretical modelling of the origin of the high activity of Pd subnanoclusters in Pd/CALB-P. a, Illustration of the model for partially oxidized Pd(111). **b**, Free-energy profiles for the (S)-1-PEA racemization on pristine Pd(111) and partially oxidized Pd(111) surfaces.

finally recovers to PEA with the R or S configuration. The calculated free-energy profiles indicate that the partially oxidized Pd(111) renders a higher catalytic activity with a lower desorption energy (PEA* → PEA) (by 0.39 eV) and lower dehydrogenation/hydrogenation reaction energy (PEA* → intermediate → PEA*) (by 0.15 eV), compared to that on the pristine Pd(111). The high desorption energy of PEA on pristine Pd(111) is considered to be the reason why a high temperature is required for catalysis using the commercial Pd/C (ref. [4]). As the Pd surface with partial oxidation results in a lower desorption energy, Pd/CALB-P can perform efficiently at a lower temperature. Given that the role of the solvent obtained

a similar result (Supplementary Fig. 33), these results suggest that the engineering of the oxidation state of Pd plays an important role in the size-dependent activity of Pd in Pd/CALB-P nanohybrids. In addition, the polar CALB-P nanoconjugate stabilizes the partially oxidized form of Pd in the non-polar toluene solvent.

The incorporation of Pd NPs within CALB-P did not affect the secondary structure of CALB (Supplementary Fig. 35). The influence of Pd NPs on the tertiary structure of CALB (Supplementary Fig. 36) might cause a reduced enzyme activity. The relative activities of lipase in xPd/CALB-P (x=2.5, 2.2, 1.6 and 0.8) in aqueous solution determined by the standard method using p-nitrophenyl
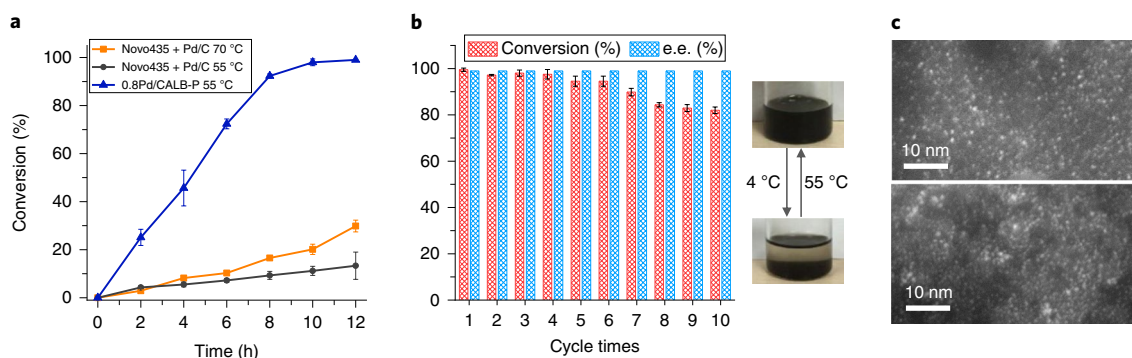
Fig. 5 | The catalytic performance and reusability of 0.8Pd/CALB-P nanohybrids for the DKR of 1-PEA. a, Catalytic performance of 0.8Pd/CALB-P at 55 °C and of a combination of commercially available Novozym 435 and Pd/C at 70 and 55 °C for the DKR reactions. **b**, Conversions and e.e. values in ten cycles of the reaction using 0.8Pd/CALB-P as the catalyst. Inset: the temperature responsiveness of Pd/CALB-P. The nanohybrids were highly dispersed in toluene at 55 °C with magnetic stirring and then precipitated when the temperature cooled down to 4 °C. Values and error bars represent the means and s.d. from at least three independent measurements. **c**, HAADF-STEM images of 0.8Pd/CALB-P before (top) and after (bottom) the cycling.

Table 1 | DKR of different amines catalysed by different hybrid catalysts.

Catalyst	Amines	Time (h)	Temperature (°C)	Yield (%)	e.e. (%)
0.8Pd/CALB-P	1	14	70	97	99
0.8Pd/CALB-P	1	12	65	99	99
0.8Pd/CALB-P	1	8	55	92	99
0.8Pd/CALB-P	1	36	45	95	99
1.6Pd/CALB-P	1	16	70	91	99
1.6Pd/CALB-P	1	14	65	93	99
1.6Pd/CALB-P	1	12	55	96	99
0.8Pd/CALB-P	2	16	55	91	99
0.8Pd/CALB-P	3	24	55	60	99
Novo435 + Pd/C	1	16	70	36	95
Novo435 + Pd/C	1	48	70	99	86
Novo435 + Pd/C	1	12	55	7	99
Novo435 + Pd/C	2	24	55	33	99
Novo435 + Pd/C	3	24	55	10	99

Reaction conditions: racemic amines **1**, **2** and **3** (0.20 mmol), ethyl acetate (0.60 mmol), toluene (2 ml) under an argon atmosphere. All the catalysts contained 1.3 mg of Pd NPs and 3.6 mg of CALB.

is that Pluronic is readily soluble in organic solvents and results in a good dispersion of enzyme–Pluronic conjugates and Pluronic–enzyme-metal nanohybrids in organic solvents (Supplementary Fig. 10). In addition, the amphiphilic property of Pluronic is helpful for the entanglement of a polymer chain around protein surface to form nanoreactors for the accommodation of Pd NPs, as shown by molecular dynamics simulations (Supplementary Fig. 14). Moreover, the amphiphilic property of Pluronic is helpful for enzyme stability in organic solvents. The hydrophilic segments create a hydrophilic microenvironment that can preserve the essential water of enzymes in organic solvents[22,41,42]. We also optimized the molecular weights of Pluronics (L121, P123, F68 and F127) to synthesize the Pd/CALB–Pluronic nanohybrids (Supplementary Table 2). As shown in the HAADF-STEM images (Supplementary Fig. 8), Pd NPs were obtained for Pd/CALB–Pluronic (L121, P123 and F68) nanohybrids and the average sizes of the Pd particles in these samples were 1.2 ± 0.4, 1.4 ± 0.5 and 1.6 ± 0.5 nm, respectively. Ultrasmall Pd clusters (<1 nm) were more easily obtained by CALB-–Pluronic (F127). More importantly, the CALB–Pluronic (F127) and Pd/CALB–Pluronic (F127) conjugates retained a higher enzymatic activity than the CALB–Pluronic (L121, P123 and F68) and Pd/CALB–Pluronic (L121, P123 and F68) conjugates (Supplementary Fig. 9). Therefore, we concluded that Pluronic F127 is an optimal choice in our study.

DKR reactions catalysed by lipase–Pd nanohybrids. At the optimum temperature (55 °C) of 0.8Pd/CALB-P indicated in Fig. 2i, the Pd-catalysed racemization of (S)-1-PEA was coupled with the lipase-catalysed acylation of (R)-1-PEA in one step to produce N-((R)-1-phenylethyl) acetamide (Supplementary Fig. 38). In the combined enzymatic and heterogeneous catalysis, the 0.8Pd/CALB-P displayed an extremely high catalytic efficiency at 55 °C compared to the combination of Novozym 435 and Pd/C at 70 and 55 °C (Fig. 5a). Within 12 hours, the 0.8Pd/CALB-P-catalysed reaction reached ~100% conversion and an enantiomeric excess (e.e.) value of >99%, with a substrate concentration of 100 mM. This process operated at a high substrate concentration comparable to previous works[13,25] is promising for the application in a practical industrial enzymatic catalysis. The combination of Novozym 435 and Pd/C only reached a 7% conversion within 12 hours under the same conditions. Previous studies on the DKR of amines usually required more than 16 hours at 70 °C to achieve an over 90% conversion, even with the assistance of H_2 to promote the Pd activity[43–45]. Here, owing to the high activity of Pd subnanoclusters in 0.8Pd/CALB-P, a 92% conversion was achieved within eight hours a at relatively

butyrate as the substrate at 25 °C were 44.5, 46.7% 78.8 and 80.5% respectively, compared with native CALB at the same protein amount (Supplementary Fig. 41). In the kinetic resolution of (±)-1-PEA in toluene at 70 °C, 0.8Pd/CALB-P exhibited an approximately 3.6- and 1.9-times apparent activity of free CALB and commercial immobilized lipase Novozym 435, respectively (Supplementary Fig. 37). As the free CALB molecules were severely aggregated in organic solvents, the high apparent activity of CALB in xPd/CALB-P in toluene was a result of the highly dispersed form of xPd/CALB-P with the assistance of Pluronic conjugation[22]. The commercialized Novozym 435 is established as an excellent immobilized lipase that displays a high activity and stability in organic solvents[39,40]. Here, at temperatures of 45–70 °C (Fig. 2i), the highly dispersed 0.8Pd/CALB-P exhibited 1.3–1.8 times the activity of Novozym 435.

Owing to the hydrophilicity of most polyelectrolytes, protein polyelectrolyte complexes[23–25] effectively improve enzyme activity and stability in aqueous solution. Here the advantage of our strategy

low temperature (55 °C) without H_2. Comparably high activities of a lipase–Pd nanohybrid[13] and nano-Pd in mesocellular foam[27] were previously reported by the Bäckvall group. For the thermal stability of the enzyme, the 0.8Pd/CALB-P nanohybrid reserved 41% of the initial enzymatic activity after incubation at 55 °C for one week, which was comparable with that of Novozym 435 (a remaining 42% of the initial activity) (Supplementary Fig. 43). Additionally, the Pd/CALB-P nanohybrids were temperature responsive and can be precipitated at room temperature after reaction and easily recovered by centrifugation[22] (Fig. 5b). The 0.8Pd/CALB-P exhibited more than an 80% residual activity and a greater than 99% e.e. value for ten batches of reuse without detachment or aggregation of the Pd NPs (Fig. 5b,c). Enantiopure amines are highly valuable products and key intermediates for chiral pharmaceuticals, agrochemicals and functional materials. Generally, strategies, which include chemical synthesis, biocatalytic asymmetric synthesis[42] and chemoenzymatic synthesis, are applied in the production of chiral amines. In this study, besides (±)-1-PEA (amine **1**), other amine intermediates, such as (±)-1-aminoindan (amine **2**) and (±)-1,2,3,4-tetrahydro-1-naphthylamine (amine **3**) (Table 1) were also utilized to evaluate the efficiency of Pd/CALB-P. (*R*)-1-aminoindan is the intermediate of rasagiline for the treatment of Parkinson's disease, and (*R*)-1,2,3,4-tetrahydro-1-naphthylamine is the intermediate of apoptosis protein inhibitor modulator for cancer treatment. Pd/CALB-P with smaller Pd sizes showed a significantly enhanced catalytic efficiency in the DKR of these amines and produced chiral products with high yields and e.e. values (Table 1). For all the amines investigated, Pd/CALB-P exhibited a higher activity than the combination of Novozym 435 and Pd/C. The results suggest that the close match of enzymatic and heterogeneous catalysis plays a very important role in developing highly efficient, integrated cascade reactions.

Conclusions

A single protein–polymer conjugate was used as a confined nanoreactor to synthesize the enzyme–metal nanohybrid with a controllable metal NP size. The protein–polymer conjugate effectively inhibited the aggregation between metal clusters during the metal crystal growth, and therefore produced a confined Pd subnanocluster down to 0.8 nm. The partially oxidized form of the Pd subnanoclusters contributed to the greatly enhanced catalytic activity of Pd in the nanohybrids. This design of lipase–Pd nanohybrids allowed the Pd activity and lipase activity to be closely matched at a relatively low temperature, which results in an increased efficiency in the combined enzymatic and heterogeneous catalysis. We suggest that this study provides a promising strategy to construct enzyme–metal hybrid catalysts for enzymatic and heterogeneous cascade reactions.

Methods

Preparation of Pd/CALB-P nanohybrids. Palladium acetate was dissolved at different concentrations in methanol (2 ml) and then added into the CALB-P aqueous solution (phosphate buffer, 8 ml, 50 mM, pH 7.0) under magnetic stirring at 25 °C. The concentrations of $Pd(OAc)_2$ and CALB-P in the synthesis of the Pd/CALB-P nanohybrids with different NP sizes are shown in Supplementary Table 5. The reaction solution was stirred for 20 h followed by dialysis against phosphate buffer (10 mM, pH 7.0) at 4 °C overnight. The powder of the nanohybrids was obtained by lyophilization and stored in a desiccator. Before characterization and utilization, the dry powder of the Pd/CALB-P nanohybrids (30 mg) was resuspended in toluene (3 ml) and reduced by $NaBH_4$ (31.7 μmol) under magnetic stirring at 25 °C for 3 h. The precipitated nanohybrids were collected by centrifugation and washed with toluene three times. A powder of the Pd/CALB-P nanohybrids was obtained by drying under vacuum at 35 °C overnight and then it was stored in vacuum oven. Owing to the intrinsic properties of Pluronic[22], Pd/CALB-P nanohybrids were readily dispersed in toluene at 55 °C and were conveniently recovered by precipitation at 4 °C. Supplementary Methods gives details of the synthesis and characterization of metal/CALB-P nanohybrids.

DKR of amines. In a typical reaction, 0.8Pd/CALB-P (37 mg, 9.8 wt% CALB, 3.603 wt% Pd) was dispersed in dry toluene (2 ml) and added to a 25 ml stainless autoclave. Racemic amines (0.2 mmol) and ethyl acetate (60 μl, 0.6 mmol) were

added to the reaction mixture. The autoclave was evacuated and filled with argon three times. The reaction was stirred at the indicated temperature under a 0.4 MPa argon atmosphere and sampled periodically. The e.e. values and the conversions were monitored by chiral HPLC analysis. The catalytic performance of the Pd/CALB-P nanohybrids was compared to that of the combination of commercially available Novozym 435 (18.5 mg) and Pd/C (13.3 mg, 10 wt% Pd) at the indicated conditions. For the recycling use of 0.8Pd/CALB-P, after the reaction mixture was cooled to room temperature (25 °C) and the precipitated nanohybrids were separated by centrifugation at 10,000 revolutions per minute at 4 °C for 10 min. After washing with cool toluene three times, the precipitated nanohybrids were transferred to a 25 ml stainless-steel autoclave and resuspended in toluene at 55 °C by magnetic stirring to carry out the next run of catalysis.

NanoESI–MS. The nanoESI source consisted of a pulled glass capillary with an inserted steel wire (~4 cm in length) and 0.9–3.5 KV of applied voltage. Borosilicate glass capillary tips (1.5 mm outer diameter and 0.86 mm inner diameter) (Sutter Instrument) was pulled using a P-1000 Flaming/Brown micropipette puller (Sutter Instrument) to a tip approximately 1 μm in diameter. The sample solution was pumped by the micropump (KD Scientific) with a 1 ml syringe (Hamilton), which was connected by the fused silica capillary between the needle and the nano capillary probing. Different high voltages were applied on the needle to form the microdroplet at the tip of nanoESI. The flow rate was precisely set to 5 μl min⁻¹ by the micropump. The nanoESI solutions were ammonium acetate solutions with a concentration ratio of 20/1 between the protein solution and the trypsin solution unless otherwise specified. An LTQ Orbitrap Velos mass spectrometer (Thermo Scientific) was employed to carry out the ambient MS analysis. At the stage of condition optimization, this was operated in the full scan mode from 200 to 2,000 *m/z*. The MS capillary temperature was set at 275 °C with an S-lens voltage of 55 V. The protein sample was dissolved in 5 mM ammonium acetate solution at pH 6.0 and the final concentration was 5–20 μM unless specifically noted.

DFT calculations. All the DFT calculations were performed with the Vienna ab initio simulation package[46–48] using the Perdew–Burke–Ernzerhof flavour[49] of DFT and the projector augmented wave method[50]. The valence electrons were described by plane-wave basis sets with a plane-wave cut-off energy of 400 eV, and the reciprocal space was sampled by only the Γ point. The Pd surface slabs were constructed using the experimental lattice parameter of 3.859 Å. Two models of Pd catalysts were constructed, Pd(111) and the partially oxidized Pd(111). In partially oxidized Pd(111) model, an O atom was inserted into the tetrahedral centre below each Pd atom of the first layer. For both models, four layers of (6 × 6) Pd(111) were used, with a vacuum layer of 20 Å. Only the two top layers were fully relaxed, whereas the two bottom layers were fixed during the geometry optimizations. For the partially oxidized Pd(111), the oxygen layer was also fully relaxed. The convergence criteria were set to 1×10^{-5} eV energy differences to solve the electronic wavefunctions for the local minima initial states, intermediate states and final states. All the initial, intermediate and final state geometries (atomic coordinates) were converged to within 1×10^{-2} eV Å⁻¹ for the maximal components of forces. The free energies at the reaction temperature (328.15 K) were calculated with equation (1):

$$G = E_{DFT} + ZPE + \delta H_0 - T_S \tag{1}$$

where E_{DFT}, ZPE, δH_0 and T_S are the total energy from the DFT calculations, the zero point energy, the integrated heat capacity and the entropy contribution. The relevant thermodynamic data of all the reaction species and adsorption conformation for them are given in Supplementary Table 9 and Supplementary Figs. 31 and 32. All the optimized structures are given in Supplementary Data 1–4.

Data availability

The data that support the plots within this paper and other findings of this study are available from the corresponding author upon request.

References

1. Ye, R., Zhao, J., Wickemeyer, B. B., Toste, F. D. & Somorjai, G. A. Foundations and strategies of the construction of hybrid catalysts for optimized performances. *Nat. Catal.* **1**, 318–325 (2018).
2. Litman, Z., Wang, Y., Zhao, H. & Hartwig, J. F. Cooperative asymmetric reactions combining photocatalysis and enzymatic catalysis. *Nature* **560**, 355–359 (2018).
3. Dydio, P. et al. An artificial metalloenzyme with the kinetics of native enzymes. *Science* **354**, 102–106 (2016).
4. Verho, O. & Bäckvall, J. E. Chemoenzymatic dynamic kinetic resolution: a powerful tool for the preparation of enantiomerically pure alcohols and amines. *J. Am. Chem. Soc.* **137**, 3996–4009 (2015).

5. Efrati, A. et al. Assembly of photo-bioelectrochemical cells using photosystem I-functionalized electrodes. *Nat. Energy* **1**, 15021–15027 (2016).

6. Zhang, H. et al. Bacteria photosensitized by intracellular gold nanoclusters for solar fuel production. *Nat. Nanotechnol.* **13**, 900–905 (2018).

7. Rudroff, F. et al. Opportunities and challenges for combining chemo- and biocatalysis. *Nat. Catal.* **1**, 12–22 (2018).

8. Denard, C. A. et al. Cooperative tandem catalysis by an organometallic complex and a metalloenzyme. *Angew. Chem. Int. Ed.* **126**, 475–479 (2014).

9. Denard, C. A., Hartwig, J. F. & Zhao, H. Multistep one-pot reactions combining biocatalysts and chemical catalysts for asymmetric synthesis. *ACS Catal.* **3**, 2856–2864 (2013).

10. Groeger, H. & Hummel, W. Combining the 'two worlds' of chemocatalysis and biocatalysis towards multi-step one-pot processes in aqueous media. *Curr. Opin. Chem. Biol.* **19**, 171–179 (2014).

11. Fu, H. et al. Chemoenzymatic asymmetric synthesis of the metallo-β-lactamase inhibitor aspergillomarasmine A and related aminocarboxylic acids. *Nat. Catal.* **1**, 186–191 (2018).

12. Reetz, M. T. & Schimossek, K. Lipase-catalyzed dynamic kinetic resolution of chiral amines: use of palladium as the racemization catalyst. *CHIMIA* **50**, 668–669 (1996).

13. Engström, K. et al. Co-immobilization of an enzyme and a metal into the compartments of mesoporous silica for cooperative tandem catalysis: an artificial metalloenzyme. *Angew. Chem. Int. Ed.* **52**, 14006–14010 (2013).

14. Kim, M. J. et al. Dynamic kinetic resolution of primary amines with a recyclable Pd nanocatalyst for racemization. *Org. Lett.* **9**, 1157–1159 (2007).

15. Paetzold, J. & Bäckvall, J. E. Chemoenzymatic dynamic kinetic resolution of primary amines. *J. Am. Chem. Soc.* **127**, 17620–17621 (2005).

16. Thalén, L. K. et al. A chemoenzymatic approach to enantiomerically pure amines using dynamic kinetic resolution: application to the synthesis of norsertraline. *Chem. Eur. J.* **15**, 3403–3410 (2009).

17. Parvulescu, A. N., Jacobs, P. A. & De Vos, D. E. Heterogeneous Raney nickel and cobalt catalysts for racemization and dynamic kinetic resolution of amines. *Adv. Synth. Catal.* **350**, 113–121 (2008).

18. Blacker, A. J., Stirling, M. J. & Page, M. I. Catalytic racemisation of chiral amines and application in dynamic kinetic resolution. *Org. Process. Res. Dev.* **11**, 642–648 (2007).

19. Strohmeier, G. A. et al. Application of designed enzymes in organic synthesis. *Chem. Rev.* **111**, 4141–4164 (2011).

20. Renata, H., Wang, Z. J. & Arnold, F. H. Expanding the enzyme universe: accessing non-natural reactions by mechanism-guided directed evolution. *Angew. Chem. Int. Ed.* **54**, 3351–3367 (2015).

21. Sheldon, R. A. & van Pelt, S. Enzyme immobilisation in biocatalysis: why, what and how. *Chem. Soc. Rev.* **42**, 6223–6235 (2013).

22. Zhu, J. et al. Temperature-responsive enzyme–polymer nanoconjugates with enhanced catalytic activities in organic media. *Chem. Commun.* **49**, 6090–6092 (2013).

23. J. Thiele, M. et al. Enzyme–polyelectrolyte complexes boost the catalytic performance of enzymes. *ACS Catal.* **8**, 10876–10887 (2018).

24. vander Straeten, A. et al. Protein–polyelectrolyte complexes to improve the biological activity of proteins in layer-by-layer assemblies. *Nanoscale* **9**, 17186–17192 (2017).

25. Zhang, Y., Wang, Q. & Hess, H. Increasing enzyme cascade throughput by pH-engineering the microenvironment of individual enzymes. *ACS Catal.* **7**, 2047–2051 (2017).

26. Cheng, H. et al. Combination cancer treatment through photothermally controlled release of selenous acid from gold nanocages. *Biomaterials* **178**, 517–526 (2018).

27. Gustafson, K. P., Lihammar, R., Verho, O., Engström, K. & Bäckvall, J. E. Chemoenzymatic dynamic kinetic resolution of primary amines using a recyclable palladium nanoparticle catalyst together with lipases. *J. Org. Chem.* **79**, 3747–3751 (2014).

28. Xu, G., Dai, X., Fu, S., Wu, J. & Yang, L. Efficient dynamic kinetic resolution of arylamines with Pd/layered double-hydroxide-dodecyl sulfate anion for racemization. *Tetrahedron Lett.* **55**, 397–402 (2014).

29. Vasan, H. N. & Rao, C. N. R. Nanoscale Ag–Pd and Cu–Pd alloys. *J. Mater. Chem.* **5**, 1755–1757 (1995).

30. Ayyappan, S. et al. Nanoparticles of Ag, Au, Pd, and Cu produced by alcohol reduction of the salts. *J. Mater. Res.* **12**, 398–401 (1997).

31. Xie, J., Zheng, Y. & Ying, J. Y. Protein-directed synthesis of highly fluorescent gold nanoclusters. *J. Am. Chem. Soc.* **131**, 888–889 (2009).

32. Tan, Y. N., Lee, J. Y. & Wang, D. I. C. Uncovering the design rules for peptide synthesis of metal nanoparticles. *J. Am. Chem. Soc.* **132**, 5677–5686 (2010).

33. Selvakannan, P. R. et al. Capping of gold nanoparticles by the amino acid lysine renders them water-dispersible. *Langmuir* **19**, 3545–3549 (2003).

34. Filice, M., Marciello, M., del Puerto Morales, M. & Palomo, J. M. Synthesis of heterogeneous enzyme–metal nanoparticle biohybrids in aqueous media and their applications in C–C bond formation and tandem catalysis. *Chem. Commun.* **49**, 6876–6878 (2013).

35. Görbe, T. et al. Design of a Pd(0)–CalB CLEA biohybrid catalyst and its application in a one-pot cascade reaction. *ACS Catal.* **7**, 1601–1605 (2017).

36. Schüth, F., Ward, M. D. & Buriak, J. M. Common pitfalls of catalysis manuscripts submitted to chemistry of materials. *Chem. Mater.* **30**, 3599–3600 (2018).

37. Yu, H. et al. The XAFS beamline of SSRF. *Nucl. Sci. Technol.* **26**, 050102 (2015).

38. Lee, J. H. et al. Chemoenzymatic dynamic kinetic resolution of alcohols and amines. *Eur. J. Org. Chem.* **2010**, 999–1015 (2010).

39. Eigtved, P. Immobilization of lipase by adsorption on a particulate macroporous. US patent No. 5,156,963 (1992).

40. Adlercreutz, P. Immobilisation and application of lipases in organic media. *Chem. Soc. Rev.* **42**, 6406–6436 (2013).

41. Zaks, A. & Klibanov, A. M. The effect of water on enzyme action in organic media. *J. Biol. Chem.* **263**, 8017–8021 (1988).

42. Wu, X., Yang, C. & Ge, J. Green synthesis of enzyme/metal–organic framework composites with high stability in protein denaturing solvents. *Bioresour. Bioproc.* **4**, 24 (2017).

43. Parvulescu, A., De Vos, D. & Jacobs, P. Efficient dynamic kinetic resolution of secondary amines with Pd on alkaline earth salts and a lipase. *Chem. Commun.* **42**, 5307–5309 (2005).

44. Parvulescu, A. N., Jacobs, P. A. & De Vos, D. E. Palladium catalysts on alkaline-earth supports for racemization and dynamic kinetic resolution of benzylic amines. *Chem. Eur. J.* **13**, 2034–2043 (2007).

45. Jin, Q. et al. Modification of supported Pd catalysts by alkalic salts in the selective racemization and dynamic kinetic resolution of primary amines. *Catal. Sci. Technol.* **4**, 464–471 (2014).

46. Kresse, G. & Hafner, J. Ab initio molecular dynamics for liquid metals. *Phys. Rev. B* **47**, 558–561 (1993).

47. Kresse, G. & Furthmüller, J. Efficiency of ab-initio total energy calculations for metals and semiconductors using a plane-wave basis set. *Comp. Mater. Sci.* **6**, 15–50 (1996).

48. Kresse, G. & Furthmüller, J. Efficient iterative schemes for ab initio total-energy calculations using a plane-wave basis set. *Phys. Rev. B* **54**, 11169–11186 (1996).

49. Perdew, J. P., Burke, K. & Ernzerhof, M. Generalized gradient approximation made simple. *Phys. Rev. Lett.* **77**, 3865–3868 (1996).

50. Kresse, G. & Joubert, D. From ultrasoft pseudopotentials to the projector augmented-wave method. *Phys. Rev. B* **59**, 1758–1775 (1999).

Acknowledgements

Author contributions

J.G., H.X. and R.N.Z. supervised the project. J.G. and X.L. conceived the idea. X.L. performed the experiments with technical help from Y.S. and J.X. Y.C performed the calculations. K.L. performed the mass spectra analyses. J.M., Z.L. and J.L. participated in analysing the results. X.L., L.W., J.G., H.X. and R.N.Z. co-wrote the paper.

Competing interests

The authors declare no competing interests.

Additional information

Supplementary information is available for this paper at https://doi.org/10.1038/s41929-019-0305-8.

Reprints and permissions information is available at www.nature.com/reprints.

Correspondence and requests for materials should be addressed to J.G., H.X. or R.N.Z.

Publisher's note: Springer Nature remains neutral with regard to jurisdictional claims in published maps and institutional affiliations.